Surface summertime radiative forcing by shallow cumuli at the Atmospheric Radiation Measurement Southern Great Plains site

Larry K. Berg,[1] Evgueni I. Kassianov,[1] Charles N. Long,[1] and David L. Mills Jr.[2]

Received 8 June 2010; revised 27 September 2010; accepted 15 October 2010; published 8 January 2011.

[1] Although shallow cumuli are common over large areas of the globe, their impact on the surface cloud radiative forcing (CRF) has not been carefully evaluated. This study addresses this shortcoming by analyzing data collected during conditions with single-layer shallow cumuli over eight summers (2000 through 2007) at the U.S. Department of Energy Atmospheric Radiation Measurement (ARM) Southern Great Plains (SGP) site. During periods with clouds, the average shortwave and longwave CRF at the surface are −45.5 W m^{-2} (out of 612 W m^{-2} estimated for clear-sky conditions) and +15.9 W m^{-2} (out of −105.2 W m^{-2} estimated for clear-sky conditions), respectively. Instances of cloud-induced enhancement of the shortwave irradiance over that estimated for clear skies are observed approximately 20% of the time and are caused by spatial and temporal inhomogeneity of cumuli. Such enhancement is responsible for occurrences of positive shortwave CRF with instantaneous values as large as +75 W m^{-2}. The total amount of shortwave and longwave energy deposited at the surface over a period of time depends nonlinearly on the fractional sky cover, and the largest values of the deposited energy occur for intermediate cloud amounts between 0.4 and 0.6.

Citation: Berg, L. K., E. I. Kassianov, C. N. Long, and D. L. Mills Jr. (2011), Surface summertime radiative forcing by shallow cumuli at the Atmospheric Radiation Measurement Southern Great Plains site, *J. Geophys. Res.*, *116*, D01202, doi:10.1029/2010JD014593.

1. Introduction and Motivation

[2] The Earth's radiation budget is primarily modulated by clouds; therefore, understanding the interaction of clouds and radiation is one of the most important problems in climate-related studies [*Forster et al.*, 2007]. Typically, bulk cloud-induced changes of the radiation budget are described by the cloud radiative forcing (CRF), which is the difference between radiative fluxes obtained under all-sky and clear-sky conditions [e.g., *Ramanathan et al.*, 1989]. Satellite and ground-based observations provide estimates of the CRF at the top of the atmosphere (TOA) and surface, respectively. For example, *Mace et al*. [2006] derived both surface and TOA CRF for overcast cases. Observations and model results reveal that the CRF depends on cloud type and can be positive or negative [*Sengupta et al.*, 2004; *Dupont and Haeffelin*, 2008; *Ghate et al.*, 2009], indicating that different cloud types can cool (negative CRF) or warm (positive CRF) the earth-atmosphere system. The largest negative values of surface CRF are commonly observed for low and almost overcast optically thick clouds with large horizontal extent such as marine stratocumulus, which reflect most of the incoming solar radiation [e.g., *Ghate et al.*, 2009].

[3] Different cloud types are characterized by distinctive temporal and spatial variability of their geometric and optical properties. Large variations of cloud properties are responsible for significant fluctuations of the surface solar irradiance. Compared to the clear-sky irradiance, the all-sky irradiance may have a large reduction or enhancement in areas of shadow (obscured Sun) or sunlight (unobscured Sun), respectively. In other words, all-sky values may exceed the corresponding clear-sky values during periods with inhomogeneous clouds. Such cloud-induced enhancement is an interesting feature associated with cloud inhomogeneity and has been a focus of many studies [e.g., *Franceschini*, 1968; *Wen et al.*, 2001; *Wyser et al.*, 2002; *Pfister et al.*, 2003]. In particular, *Pfister et al.* [2003] used a 1 year record of total, opaque, and thin cloud fraction and the corresponding solar irradiance to illustrate that the cloud-induced enhancement is on average 10% larger than the clear-sky flux and occurs 5% of the time. Similar to other studies, they also demonstrated that both the magnitude and frequency of the enhancement depend on the cloud fraction and the averaging time. We emphasize that these statistics presented by *Pfister et al*. [2003] represent the combined effect of clouds with different optical and geometrical properties.

[1]Pacific Northwest National Laboratory, Richland, Washington, USA.
[2]Department of Computer Science and Engineering, University of South Carolina, Columbia, South Carolina, USA.

0148-0227/11/2010JD014593

[4] Fair weather cumuli are ubiquitous, occurring over large portions of both the continents and trade wind regions of the oceans [e.g., *Warren et al.*, 1988; *Hahn and Warren*, 1999; *Rauber et al.*, 2007], and they may have a substantial impact on the surface radiation budget [e.g., *Lane et al.*, 2002]. Compared to other cloud types, cumulus properties have the largest variations in both time and space and these variations are poorly captured by current large-scale models [e.g., *Xie et al.*, 2010]. Since these variations are also difficult to monitor and accurately describe, efforts to improve the representation of these clouds have been hampered, in part, by the lack of appropriate observational constraints that relate cumulus properties to the radiative fluxes.

[5] A number of studies [e.g., *Stull*, 1992; *Lane et al.*, 2002; *Berg and Kassianov*, 2008] have documented the cloud amount associated with shallow cumuli over the central United States, but these studies did not investigate the shortwave or longwave CRF associated with these clouds. Several short-duration field campaigns were performed recently that were designed to investigate various aspects of the life-cycle of shallow cumuli, including the Gulf of Mexico Atmospheric Composition and Climate Study (GoMACCS) [*Jiang et al.*, 2008], the Cloud and Land Surface Interaction Campaign (CLASIC) [*Miller et al.*, 2007] and the Cumulus Humilis Aerosol Processing Study (CHAPS) [*Berg et al.*, 2009]. CLASIC was designed to examine relationships between surface processes and shallow cumuli over Oklahoma [*Miller et al.*, 2007], while CHAPS was intended to study changes of optical and chemical properties of particles as they move through shallow cumuli as well as changes of cloud microphysical properties in the vacinity of Oklahoma City [*Berg et al.*, 2009]. The study presented here represents a multiyear climatology of cumulus radiative properties that utilizes a high-resolution time series of sky cover and surface fluxes collected during eight summers (2000–2007) at the U.S. Department of Energy Atmospheric Radiation Measurement (ARM) Southern Great Plains (SGP) Site. We use these time series to address three questions: (1) How large are contributions of the shortwave and longwave components to the net CRF at the surface? (2) What is the magnitude and observational frequency of the positive shortwave CRF at the surface? (3) What is the relationship between the sky cover and the total amount of shortwave and longwave energy deposited at the surface over a period of time?

[6] We describe (section 2) and illustrate (section 3) our methodology for obtaining both instantaneous and averaged radiative properties of shallow cumuli. The results and the corresponding discussion are presented in sections 3 and 4, respectively. Our results are summarized in section 5.

2. Methodology

[7] This study uses data collected at the ARM SGP site that combines observations from an extensive set of instruments for measuring downwelling radiation and cloud macroscale properties, such as cloud fraction, cloud base height, and cloud top height. The site is located in north-central Oklahoma and is representative of the interior regions of many continents, where shallow cumuli form regularly during quiet synoptic conditions with strong surface forcing and well-developed boundary layers. Since summertime (defined here as May through August, inclusive) is a favorable time for the development of shallow cumuli and long-term summertime macroscale properties of cumuli are available [*Berg and Kassianov*, 2008], only summertime conditions are considered here. Multilayer clouds occur frequently over the ARM SGP during the summer. To select appropriate periods with single-layer shallow cumuli, a time series of cloud boundaries determined from combined radar-lidar observations [*Clothiaux et al.*, 2000] and all-sky movies produced by a Total Sky Imager (TSI) were analyzed. Such a selection process is described in detail by *Berg and Kassianov* [2008] and is designed to remove periods with stratocumulus or extensive amounts of midaltitude or high-altitude clouds. Using their methodology, the cloud fraction and cloud base height derived from radar lidar observations can be used to identify cases with multilayer clouds. Specifically, the cloud fraction computed for instances in which the cloud base heights are less than 3 km is compared with the cloud fraction computed for all clouds. If the difference between these two measures is greater than 0.1, then it is assumed that there are significant amounts of midlatitude or high-altitude clouds and that period is not considered in the subsequent analysis. A review of the cloud radar-lidar data from the eight summers yields 201 days with periods of at least 2 h of single-layer shallow cumuli. No requirement was applied in regards to the temporal continuity of the clouds. In other words, periods with shallow cumuli could be separated by periods without clouds. These clear periods that occur between cloudy periods have been excluded from the analysis. The clouds could occur at any time of the day (or night), given the focus on shallow cumuli, however, 90% of the observations are between 10:00 and 20:00 CST. It is important to note that, the cloudy periods defined in this study include times when clouds are present but the direct solar beam reaches the radiometer on the surface. The cloudy periods are not limited to only periods during which clouds block the direct solar beam.

[8] For selected cloudy periods, we estimate the CRF as the difference between the net all-sky flux (F) and its clear-sky counterpart (F_0) [e.g., *Fairall et al.*, 2008],

$$\mathrm{CRF}_x = F_x - F_{x,0}, \tag{1}$$

where subscript x = SW or x = LW indicates the shortwave and longwave radiation, respectively. These all-sky and clear-sky fluxes are obtained with a temporal resolution of 1 min. In addition to the CRF computed using (1), the total energy deposited (TED_x) on the surface can be computed by integrating F_{SW} or F_{LW} during cloudy periods. The TED_x defines the cloud impact on the surface energy budget and is the amount of energy that is ultimately available for partitioning between sensible, latent, and the soil heat flux. The TED_x has units of J m^{-2}. Alternatively, the TED_x can be expressed in terms of kWh m^{-2}, which is commonly used in the solar power industry to evaluate the potential solar energy resource for a given geographic location. The change in the total energy deposited ($\Delta\mathrm{TED}_x$) due to the shallow

clouds is computed by integrating the 1 min values of F_x over all hours with clouds, using

$$\Delta \mathrm{TED}_x = \int_C (F_x - F_{x,0}) H(t) \mathrm{d}t, \quad (2)$$

where $H(t)$ is the Heaviside step function which is defined to be 1 during cloudy periods and 0 at other times. One advantage of ΔTED_{SW} and ΔTED_{LW} is that they account for both the magnitude of the forcing, as well as the number of occurrences. Measures of the impact of clouds similar to ΔTED_{SW} and ΔTED_{LW} have been suggested by *Warren and Hahn* [2002], who defined the average cloud amount, as the product of the frequency of occurrence and the amount when present.

[9] Equation (1) contains the net fluxes $F_x = F_x^{\downarrow} - F_x^{\uparrow}$ and $F_{x,0} = F_{x,0}^{\downarrow} - F_{x,0}^{\uparrow}$, where the arrows indicate upwelling (↑) or downwelling (↓) irradiances. The shortwave transmissivity is defined as the ratio of the all-sky to clear-sky fluxes: $t_{\mathrm{SW}} = F_{\mathrm{SW}}^{\downarrow}/F_{\mathrm{SW},0}^{\downarrow}$ and represents the attenuation of the solar radiation by the cloud layer. The all-sky fluxes F_{SW} and F_{LW} are measured directly by the radiometers on the surface. Determining their clear-sky counterparts is more complicated. The shortwave clear-sky flux, $F_{\mathrm{SW},0}$, is estimated by the method of *Long and Ackerman* [2000], which approximates the downwelling shortwave clear-sky irradiance, $F_{\mathrm{SW},0}^{\downarrow}$, for the period of interest from measurements made at that location on a cloud-free day in close temporal proximity. A similar approach is used for estimation of the upwelling clear-sky shortwave, $F_{\mathrm{SW},0}^{\uparrow}$ [*Long*, 2005]. The downwelling longwave irradiance, $F_{\mathrm{LW},0}^{\downarrow}$, is obtained by another technique [*Long and Turner*, 2008] that is related to the shortwave method described by *Long and Ackerman* [2000]. To account for changes in the humidity of the lower atmosphere and the formation of haze, an additional correction is applied to the clear-sky longwave estimate. The upwelling longwave component $F_{\mathrm{LW},0}^{\uparrow}$ is obtained by using a method that combines the clear-sky net shortwave and clear-sky downwelling longwave fluxes, and screen height measurements of relative humidity and wind speed as proxies for temporal changes in latent and sensible heat fluxes [*Long*, 2005]. Also, the cloudy and clear-sky fluxes are used to estimate the fractional sky cover (C). Its shortwave and longwave values (C_{SW} and C_{LW}) are defined from shortwave [*Long et al.*, 2006] and longwave [*Durr and Philipona*, 2004] fluxes, respectively. The C_{SW} represents the total sky cover, similar to that obtained from sky imagers and human observations [*Long et al.*, 2006], but since it is solar driven is only available during daylight hours. The C_{LW} is derived using broadband longwave measurements, which are inherently insensitive to emissions from high, cold clouds. Thus C_{LW} is considered a "LW effective" sky cover that represents low and middle cloudiness only (including shallow cumuli analyzed in this study), i.e., clouds that influence the longwave measurements, but is available 24 h a day. Note that the radiative fluxes (F_x,$F_{x,0}$) and C are obtained with 1 min temporal resolution.

[10] To examine the sensitivity of these properties to the temporal resolution of the data, we define them as a function of an arbitrary averaging time period. The averaged values are defined as

$$\overline{R}_x = \sum_{i=1}^{N_x} R_x(i)/N_x, \quad (3)$$

where R are the radiative properties (including CRF, F, F_0) or sky cover (C) and N is the total number of observations within that arbitrary averaging time period. The only exception to this definition is that of the average t_{SW}, which is defined as: $\overline{t}_{\mathrm{SW}} = \overline{F}_{\mathrm{SW}}^{\downarrow}/\overline{F}_{\mathrm{SW},0}^{\downarrow}$. Similar to (1), the subscript x is used to indicate either the shortwave or longwave values. To avoid situations with large amounts of missing data or periods in which clouds either form or dissipate during the time period of interest, more than 80% of 1 min averages have to be considered cloudy for that period to be included in the analysis. For example, if the averaging time period is 1 h, than at least 48 1 min averages are required for the hourly average to be computed. Excluding periods with fewer than 80% of the 1 min averages does not significantly change the sensitivity of the radiative parameters to the sky cover (section 4) but does reduce the amount of scatter in the data. The 1 h averages are used to define the summertime (defined as May–August, inclusive) average values for periods with broken clouds,

$$\langle R_x \rangle = \sum_{j=1}^{M_j} \overline{R}_x(j)/M_x \quad (4)$$

where M is the total number of 1 h averages collected during the period of this study. Similar to the definition of $\overline{t}_{\mathrm{SW}}$, the value of $\langle t_{\mathrm{SW}} \rangle$ is defined as: $\langle t_{\mathrm{SW}} \rangle = \langle \overline{F}_{\mathrm{SW}}^{\downarrow} \rangle / \langle \overline{F}_{\mathrm{SW},0}^{\downarrow} \rangle$.

3. Illustrative Case

[11] To illustrate the methodologies described in section 2, a single case has been selected from the 201 days identified with single-layer shallow cumuli. Conditions observed on 7 May 2004 are typical of observations made on days with shallow cumuli at the ARM site. On 7 May, clouds started to form near 1700 UTC and dissipated around 2300 UTC. Figure 1 shows the corresponding clear-sky and all-sky shortwave fluxes. During clear-sky periods (before 1700 UTC and after 2300 UTC), there is good agreement between the estimated and observed clear-sky and observed all-sky shortwave fluxes. Two important features, associated with the variability of cumulus properties, can be seen in Figure 1a. The first feature is the large fluctuations of the all-sky shortwave fluxes. The amplitude of the fluctuations can be as large as 800 W m^{-2} and are comparable in magnitude to the corresponding clear-sky values. The second feature is the substantial amount of cloud-induced enhancement of the diffuse component of the downwelling shortwave radiation, as shown by instances in which the all-sky shortwave flux is greater than the clear-sky shortwave flux. In some cases, the all-sky shortwave fluxes can exceed the clear-sky counterparts by more than 200 W m^{-2}. A significant amount of enhancement can be observed even for time periods with moderate-to-large values of sky cover (e.g., around 2130 UTC).

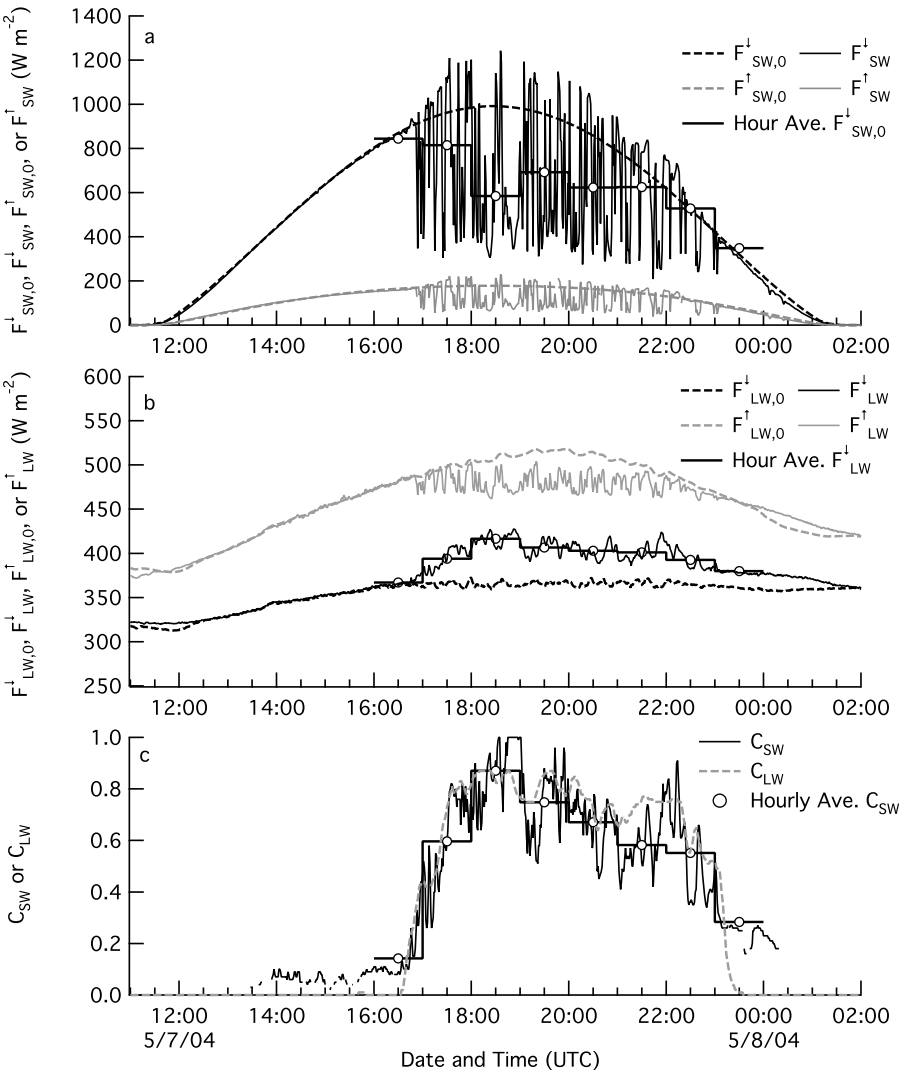

Figure 1. Time series of observed upwelling (gray) and downwelling (black) cloudy sky (solid lines) and modeled clear-sky (dashed lines) (a) shortwave and (b) longwave fluxes and (c) time series of C_{SW} and C_{LW}. Hourly average values of the downwelling shortwave and longwave fluxes and shortwave cloud fraction are indicated by the circles and thick solid lines.

[12] Similar to the results shown for shortwave radiation, there is good agreement between the observed and modeled clear-sky upwelling and downwelling longwave radiation during clear periods early in the morning and late in the afternoon (Figure 1b). The differences between the all-sky and clear-sky longwave fluxes are much smaller than the differences seen in the shortwave. For example, the difference in the upwelling longwave radiation is slightly larger than 30 W m^{-2} (a difference of approximately 7%) near 2130 UTC. The change in the downwelling longwave at the same time is about 40 W m^{-2} (a difference of approximately 10%). Both C_{SW} and C_{LW} increase quickly between 1600 and 1900 UTC, followed by a slow and relatively steady decrease until the clouds dissipate (Figure 1c). There is also generally good agreement between the two measures of cloud fraction. The CRF_{SW} has also been computed as a function of time on 7 May (Figure 2a). Similar to the shortwave fluxes (Figure 1a), there are large fluctuations in the CRF, ranging from values as small as −565 W m^{-2} to values as large as 200 W m^{-2}. The CRF_{LW} does not change sign, as only instances of positive CRF_{LW} at the surface were observed during the period with shallow cumuli (Figure 2b). In addition, the fluctuations in the longwave fluxes are smaller than the fluctuations seen for the shortwave radiation (Figures 2a and 2b). Note that the hourly averages of the longwave radiation shown in Figures 1b, 2b, and 3 include cloudy periods with fewer than 48 observations. These particular values have been included in Figures 1b, 2b, and 3 for clarity, but following the methodology described in section 2, averages with less than 80% of the total possible observations for that period are not used in any subsequent calculations. The t_{SW} shows a great deal of variability throughout the cloudy period (Figure 2c). As expected from the definition of t_{SW} given in section 2, the variations in t_{SW} are tightly coupled to variations in F_{SW} (Figures 2a and 2c). In general, t_{SW} is less than 1.0 but there are numerous occasions during which t_{SW} is greater than 1.0.

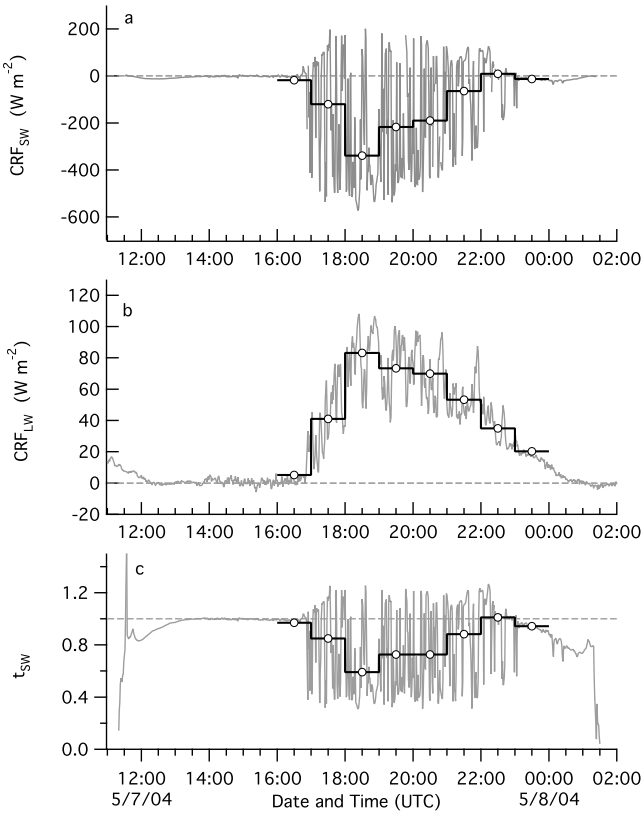

Figure 2. Time series of 1 min values of (a) CRF_{SW}, (b) CRF_{LW}, and (c) t_{SW} measured on 7 May 2004. Circles and thick solid lines indicate hourly averages.

[13] Averaging over a longer time period, in this case 1 h, removes the small-scale variations of the radiative properties (Figures 1 and 2). Within a given time period, the average values of the downwelling irradiance at the surface, $F^{\downarrow}_{SW}$, are defined by the magnitude and occurrence of the cloud-induced enhancement and reduction to the downwelling radiation as well as the time of year and time of day. Since the reduction in $F^{\downarrow}_{SW}$ occurs more often and its magnitude is typically larger (Figure 1a), the $\overline{CRF}_{SW}$ is generally negative. An exception is the time period between 2200 and 2300 UTC where the $F^{\downarrow}_{SW}$ is larger than $\overline{F}^{\downarrow}_{SW,0}$, and $\overline{CRF}_{SW}$ is observed to be positive (Figure 2a).

[14] The CRF_{SW} can be either positive or negative at any given point in time (Figure 3). Negative CRF_{SW} occurs more frequently than positive CRF_{SW}; approximately 64% of all 1 min values of CRF_{SW} observed on 7 May are negative. The magnitude of the negative CRF_{SW} is also 2–4 times larger than the positive CRF_{SW} (Figure 3). Both the negative and positive CRF_{SW} are characterized by fluctuations with a small temporal scale; the duration for the majority of both instances of positive and negative CRF_{SW} is less than 5 min (Figure 4).

[15] Generally, the negative CRF_{SW} is observed for cases when the solar disk is blocked by optically thick clouds, and thus the direct solar irradiance is substantially reduced (Figure 5). In contrast, positive CRF_{SW} is observed in broken cloud fields for cases when the direct solar beam is not blocked, and the clouds increase the diffuse radiation that reaches the surface. Changes to the surface irradiance due to cloud-induced reduction and enhancement of the surface irradiance are discussed in many studies [e.g., *Franceschini*, 1968; *Wen et al.*, 2001; *Wyser et al.*, 2002; *Pfister et al.*, 2003]. In particular, these studies show that the enhancement can exceed 20% due to the increase in diffuse radiation [*Pfister et al.*, 2003]. It has also been illustrated that the transmitted diffuse radiation is more sensitive to small-scale cloud variability than the reflected radiation [e.g., *Kassianov et al.*, 2005]. The observed sensitivity can be explained by the large contribution of the scattering component (with a few scattering events) to the diffuse irradiance. This contribution is significant for small and optically thin clouds and also for optically thin parts of large clouds. Because of the size of the cloud drops, the scattering of light by clouds is nearly independent of wavelength of the light that is being scattered compared to the scattering associated with clear-sky conditions that have a strong wavelength dependence.

[16] Both the shortwave and longwave CRF are functions of C_{SW} or C_{LW}. For the data observed on 7 May 2004, both the shortwave and longwave CRF increase in magnitude with increasing C_{SW} or C_{LW} (Figure 6), although the magnitude of the change in the shortwave CRF is much larger. Note that C_{SW} and C_{LW} shown in Figure 6 are computed from the shortwave measurements or the longwave measurements, respectively. While the maximum number of shortwave observations occurred for C_{SW} between 0.6 and 0.8 in our screened data set, the maximum number of longwave observations occurred for C_{LW} between 0.7 and 0.8, and no cases of C_{LW} greater than 0.9 were observed.

[17] While the $\overline{CRF}_{SW}$ increases in magnitude with increasing C_{SW}, the ΔTED_{SW} is largest in magnitude for C_{SW} between 0.7 and 0.8 (Figure 6c). This behavior occurs because ΔTED_{SW} takes into account both the magnitude of the forcing as well as the frequency at which that forcing occurs. In this illustrative case, ΔTED_{LW} behaves similar to the $\overline{CRF}_{LW}$ and increases in magnitude with increasing C_{LW}. As will be demonstrated in section 4, this behavior of ΔTED_{LW} is not representative of all-sky conditions

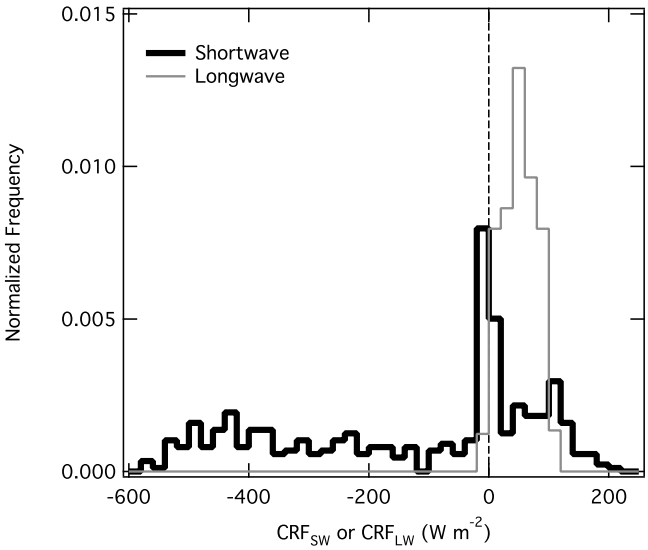

Figure 3. Histogram of CRF_{SW} (black) and CRF_{LW} (gray) computed from 1 min averages measured on 7 May 2004.

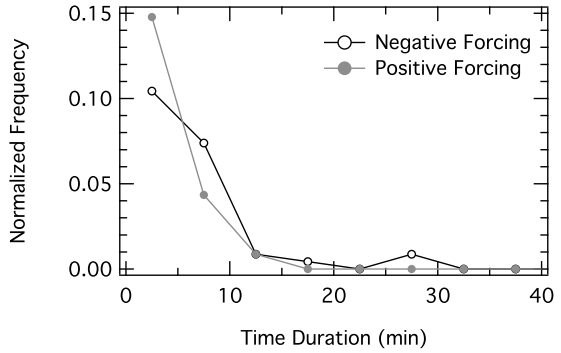

Figure 4. Time duration of periods of negative (open circles) and positive (solid circles) measured on 7 May 2004.

observed over the full period of study. In this section, the radiative forcing from the illustrative case has been documented. To evaluate the surface forcing due to shallow cumuli, the methodologies described in section 3 have been applied to all 201 days that were identified to have shallow cumuli.

4. Results

4.1. Dependence on Averaging Time

[18] Fields of shallow cumuli are not homogenous in space or time, and the solar zenith angle changes throughout the day. Because of these factors, selection of a long averaging time could lead to biases in the results. The data presented in section 3 consists of 1 min averages of CRF_{SW}, CRF_{LW}, and t_{SW} determined using equations defined in section 2. While the use of 1 min averages highlights the short time scales representative of the interactions between the clouds and the surface radiative forcing, these data exhibit substantial variability. Averaging over longer time periods reduces the scatter in both $\overline{CRF}_{SW}$ and $\overline{CRF}_{LW}$ as functions of C_{SW} and C_{LW}. For example, hourly averages of the various parameters are shown in Figures 1 and 2 for the case study presented in section 3. When 5 min averages are computed using data from all 201 days with periods of broken clouds there is still a great deal of variability in both $\overline{CRF}_{SW}$ and $\overline{CRF}_{LW}$ as a function of C_{SW} and C_{LW}, respectively (Figure 7). Therefore, it is desirable to average the observations over some longer time interval to reduce the variability. Increasing the averaging time from 5 min to 1 h reduces the scatter in $\overline{CRF}_{SW}$ and $\overline{CRF}_{LW}$ (Figure 7). There is relatively little difference in the best fit lines to the 5 min and 1 h averaged values of $\overline{CRF}_{SW}$ or $\overline{CRF}_{LW}$ shown in Figure 7. There are also only small differences in the amount of ΔTED_{SW} and ΔTED_{LW} computed from the 5 min and 1 h averages (not shown). On the basis of the results of this analysis, the 1 min observations of $\overline{CRF}_{SW}$ and $\overline{CRF}_{LW}$ are combined into 1 h averages for the rest of this analysis.

[19] Increasing the averaging time reduces the amount of data used in the analysis because there are fewer intervals in any given period, and there are fewer cases that meet the criteria for the minimum number of 1 min observations used to compute the average. For example, when 1 h averages are considered, there are 1384 possible hours, only 898 (65%)

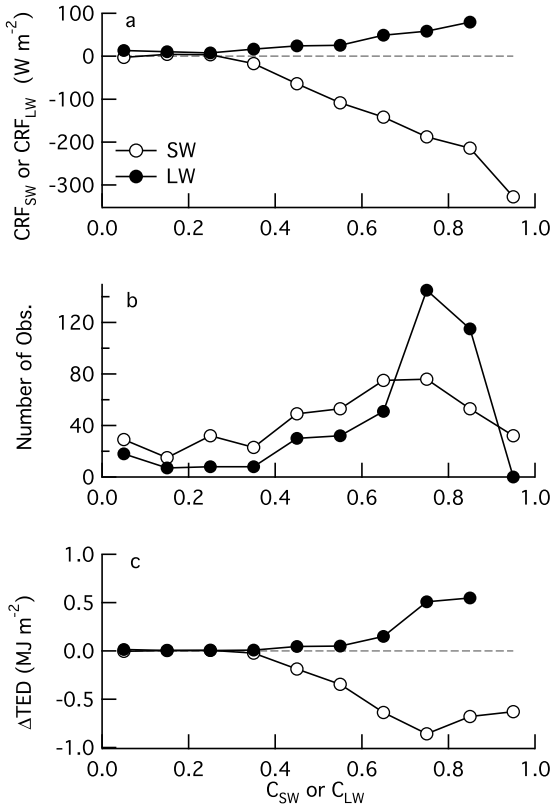

Figure 6. (a) $\overline{CRF}_{SW}$ (open circles) and $\overline{CRF}_{LW}$ (solid circles), (b) total number of shortwave (open circles) and longwave (solid circles) observations, and (c) ΔTED_{SW} (open circles) and ΔTED_{LW} (solid circles) computed for 7 May 2004.

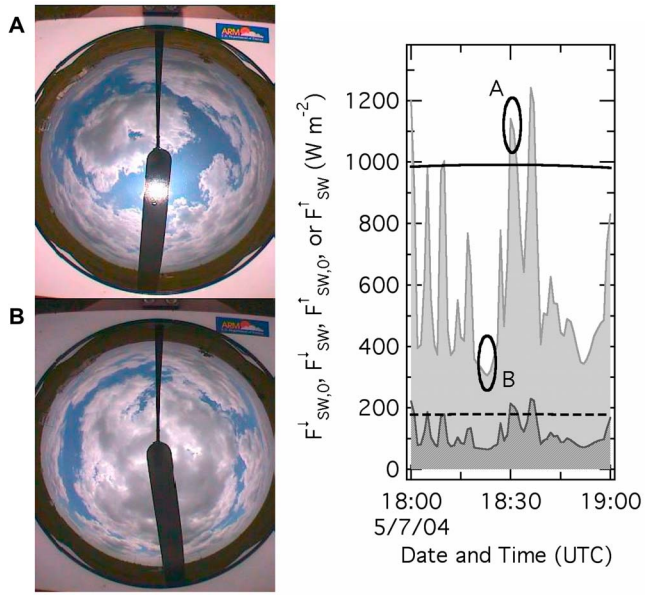

Figure 5. Total sky images taken at (a) 1830 UTC and (b) 1821 UTC on 7 May 2004. The times of these two images are highlighted on the right-hand side, which shows the time series of $F^{\uparrow}_{SW,0}$ and $F^{\downarrow}_{SW,0}$ (solid and dashed lines, respectively) and $F^{\uparrow}_{SW}$ and $F^{\downarrow}_{SW}$ (dark and light gray, respectively). Times of TSI images are indicated with tlhe Figures 5a and 5b shown on the time series.

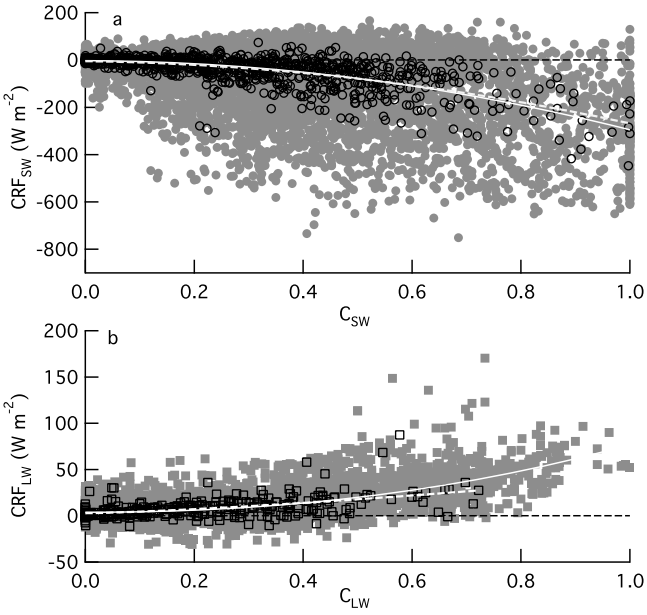

Figure 7. (a) $\overline{CRF}_{SW}$ and (b) $\overline{CRF}_{LW}$ as a function of C_{SW} and C_{LW} for averaging times of 5 min (gray symbols) and 1 h (open symbols). Best fit lines are polynomials (for shortwave) and power laws (for longwave) to both 5 min averages (white solid line) and 1 h averages (white dashed line).

of those hours are included in the shortwave analysis and 886 (64%) hours are included in the longwave analysis. In the case of 5 min averages there are 13,828 possible hours, of which 12,899 (93%) are included in the shortwave analysis, and 12,678 (93%) are used for the longwave analysis.

[20] As evident in Figure 7, there are instances of positive $\overline{CRF}_{SW}$ for averaging periods ranging from 5 min to 1 h. To investigate the magnitude of the positive and negative averages of $\overline{CRF}_{SW}$ as a function of the averaging time, periods with either positive or negative $\overline{CRF}_{SW}$ have been composited separately for averaging times ranging from 1 min to 4 h to yield averages of positive ($\overline{CRF}^{+}_{SW}$) and negative ($\overline{CRF}^{-}_{SW}$) shortwave CRF. In addition, the data have been separated into three categories of C_{SW}. These C_{SW} classes include cases in which C_{SW} is less than 0.2, between 0.2 and 0.5, and greater than 0.5. This classification system is arbitrary but yields approximately the same number of cases for small and moderate C_{SW}, but fewer cases for larger C_{SW}. The magnitude of negative and positive forcing decreases with averaging time, and is well represented with an exponential curve (Table 1 and Figure 8). The 95% confidence levels to the fits, which were computed using a Monte Carlo bootstrap method [*Press et al.*, 1996], have been included in Figure 8. Most of the change in forcing occurs for averaging times less than an hour, which is consistent with changes that are found for the duration of individual cases of positive and negative forcing in the case study (Figure 4). This result is related to the average decorrelation time of 10–15 min of the sky view from a surface site, as shown by *Kassianov et al.* [2005]. For averaging times greater than approximately 1 h, the averages of $\overline{CRF}^{+}_{SW}$ and $\overline{CRF}^{-}_{SW}$ approach an asymptotic value that is a function of the C_{SW}. It is also interesting to note that the best fit exponential curve for negative forcing and moderate sky cover reaches its asymptotic values more quickly than any of the other cases.

4.2. Summertime Averages

[21] In this study 201 days out of a total of 984 possible summertime days are identified as having time periods with single layer shallow cumuli. Thus, shallow cumuli are found to occur on about 20% of the summertime days at the ARM SGP site for the years of this study (where summertime is defined in section 2 as May through August, inclusive). The average surface shortwave and longwave CRFs have been computed (Table 2). The $\langle CRF_{SW} \rangle$ was computed following (4) and is found to be −45.5 W m^{-2} (out of a net flux of 612 W m^{-2} estimated for clear-sky conditions). The $\langle CRF_{LW} \rangle$ is found to be +15.9 W m^{-2} (out of a net flux of −105.2 W m^{-2} estimated for clear-sky conditions). Thus, the average net forcing at the surface due to shallow cumuli is −29.6 W m^{-2}. In total, shallow cumuli were observed on nearly 1300 h during the study period. The number of hours used to compute the $\langle CRF_{SW} \rangle$ or $\langle CRF_{LW} \rangle$ were reduced to 898 and 886, respectively, because of the requirement that there be 48 good values within a given hour for it to be used.

[22] Histograms of hourly averages, $\overline{CRF}_{SW}$ and $\overline{CRF}_{LW}$, have been prepared (Figure 9). The results are similar to the histograms found for the illustrative case study (Figure 3). When all 201 days with cloudy periods are considered the distribution of $\overline{CRF}_{SW}$ includes 898 values and is skewed toward negative values (skewness equal to −2.28). While the average value of $\overline{CRF}_{SW}$ is −45.5 W m^{-2}, 5% of all hourly observations are found to have $\overline{CRF}_{SW}$ smaller than −190 W m^{-2}. The majority of the observations of $\overline{CRF}_{SW}$ are negative, but 20% of all values of $\overline{CRF}_{SW}$ are greater than 0 and 5% of the hourly observations were greater than 20 W m^{-2}. The distribution of $\overline{CRF}_{LW}$ includes 886 values, is positively skewed (skewness equal to 1.70), and has a much sharper peak than is found for the distribution of $\overline{CRF}_{SW}$. A small number (less than 1%) of $\overline{CRF}_{LW}$ are slightly less than 0, and these values are most likely due to errors associated with estimating clear-sky values of $\overline{CRF}_{LW}$. For example, in the case described in section 3, the difference in clear-sky and all-sky $F^{\uparrow}_{LW}$ determined after the shallow cumuli dissipate is found to be approximately 10 W m^{-2} (Figure 1b). The average summertime value of $\langle t_{SW} \rangle$ is found to be 0.92 (Table 2).

[23] The total summertime ΔTED_{SW} (which is defined in section 2 as the change in the total energy deposited at the surface) is found to be −176 MJ m^{-2}, or −48 kW h m^{-2}. The estimated clear-sky TED_{SW} for the periods with clouds is 2837 MJ m^{-2}, so that the reduction in the TED_{SW} is 6% over the eight summers. This value is similar to the 7% reduction

Table 1. Exponential Fit Parameters for Curves of $f(C_{SW}) = A_0 + A_1 \exp(A_2 t_{ave})$ Shown in Figure 8[a]

	Negative Forcing			Positive Forcing		
	A_0	A_1	A_2	A_0	A_1	A_2
$C_{SW} < 0.2$	−15.1	−16.0	−0.0436	9.68	6.59	−0.0328
$0.2 < C_{SW} < 0.5$	−54.2	−77.9	−0.104	10.6	29.1	−0.028
$C_{SW} > 0.5$	−97.7	−109	−0.0208	−14.8	66.3	−0.0167

[a]Here t_{ave} is the averaging time.

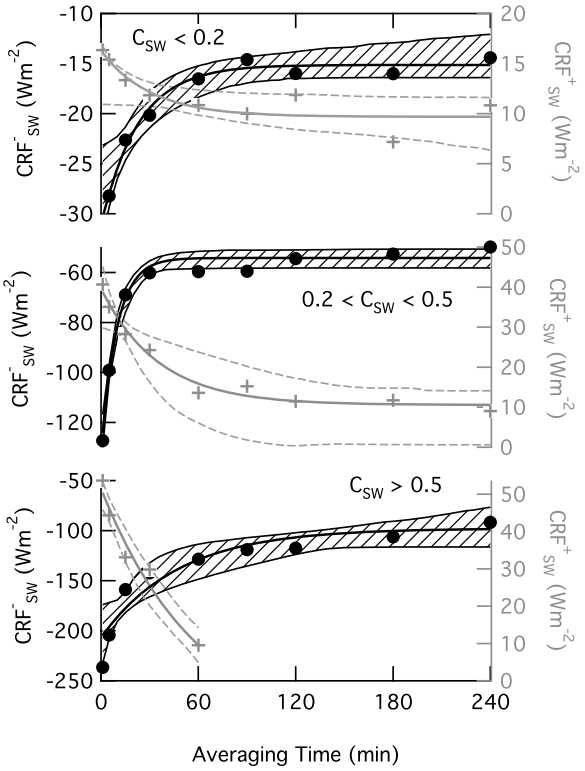

Figure 8. $\overline{CRF}^{-}_{SW}$ (black circles; left axis) and $\overline{CRF}^{+}_{SW}$ (gray crosses; right axis) for fractional sky cover (top) less than 0.2, (middle) between 0.2 and 0.5, and (bottom) greater than 0.5 as a function of the averaging time. Lines indicate exponential fit to the observations; shaded areas or dashed lines indicate 95% confidence levels to the various fits.

associated with the $\langle CRF_{SW} \rangle$. The ΔTED_{LW} is an increase of 60.0 MJ m^{-2}, while the estimated clear-sky TED_{LW} is found to be 1020 MJ m^{-2}. This increase is about 6% in the amount of downwelling longwave energy at the surface for cloudy periods. The fractional increase in TED_{LW} is smaller than the fractional change in $\langle CRF_{LW} \rangle$, which is approximately 15%. This can be explained by the associated changes in the upwelling longwave radiation. As defined in section 2, ΔTED_{LW} is the change in only the downwelling longwave radiation, while $\langle CRF_{LW} \rangle$ takes into consideration both the downwelling and upwelling radiation. In the case of $\langle CRF_{LW} \rangle$, the differences in both the upwelling and downwelling radiation play nearly equal roles in determining the $\langle CRF_{LW} \rangle$. In contrast, $\langle CRF_{SW} \rangle$ is dominated by the downwelling component because the upwelling components are small and proportional to the downwelling shortwave radiation as expressed by the surface albedo. Thus, significant differences in the ratios of ΔTED_{LW} and $\langle CRF_{LW} \rangle$ with their corresponding clear-sky values can be observed. It should be noted that 48 good observations within a given hour were required for that hour to be counted as a cloudy period and be used to compute the averages (section 2). Such a constraint was not required for ΔTED_{SW}, TED_{SW}, ΔTED_{LW}, or TED_{LW} because these radiative properties represent a temporal integration and excluding hours with less than 48 good observations would artificially reduce both quantities. Therefore, all good values of CRF_{SW} and CRF_{LW} were used to compute ΔTED_{SW} and ΔTED_{LW}.

[24] The time scale of the variability in the positive and negative shortwave forcing is also of interest. Histograms of the duration of time intervals with both negative and positive forcing are shown in Figure 10. The average duration of negative forcing is 6.5 min, while the average duration of positive forcing is 5.9 min. An exponential curve has been fit to the observations of both the intervals with negative and positive forcing. The differences between these two best fit curves are quite small, indicating that the two populations are very similar, and the differences in means of the two sets of observations are likely due to random differences. These distributions also suggest that the CRF is well described by a Poisson process and that the length of the time interval of negative and positive CRF is a random event with an exponential distribution. An additional analysis of the cumulative distributions (not shown) indicates that 95% of all periods of positive or negative forcing are less than 20 min in length. This result is in agreement with the 15 min decorrelation time scale presented by *Kassianov et al.* [2005].

[25] The number of $\overline{CRF}_{SW}$ values that are positive decreases with increasing averaging time but does not reach zero, even for averaging times as long as 4 h. When a 2 h averaging time is used, 10% (40 out of 401) of the averages are greater than 0, while when a 4 h averaging time is used, approximately 5% (9 out of 169) of the 4 h averages are found to be greater than 0 (Figure 11). The inset portion of Figure 11 was included to highlight the relatively small number of occurrences of $\overline{CRF}_{SW}$ greater than 0 for averaging times of 2 and 4 h. This behavior could be attributed, at least in part, to two factors. The first factor is associated with the uncertainty in the measured all-sky and estimated clear-sky fluxes. This is particularly true if the estimated clear-sky flux has a small positive bias. Another factor that could contribute to the occurrences of positive $\overline{CRF}_{SW}$ is the geometry of the cloud field. There could be conditions, especially when the CF is relatively small, during which relatively few cloud shadows pass over the radiometer. Thus, resulting in long periods with positive cloud forcing. Given the small number of occurrences of $\overline{CRF}_{SW}$ for an averaging time of 4 h and their small magnitude, it is unlikely that these positive $\overline{CRF}_{SW}$ for large averaging time are climatologically significant. These results should not be interpreted to imply that instances of positive CRF can be ignored when a long averaging time is applied. Rather, that the occurrence of instances of positive forcing will reduce the magnitude of the $\overline{CRF}_{SW}$ over any averaging time.

Table 2. Summertime Average Values of $\langle CRF_{SW} \rangle$, $\langle CRF_{LW} \rangle$, and $\langle t_{SW} \rangle$ Associated With Shallow Cumuli and All Summertime Clouds Obtained From *Dong et al.* [2006][a]

	Shallow Cumuli	All Low Clouds
$\langle CRF_{SW} \rangle$	−45.5 (612)	−87.6 (260.1)
$\langle CRF_{LW} \rangle$	+15.9 (−105.2)	+40.7 (−74.1)
$\langle t_{SW} \rangle$	0.92	

[a]Values in parentheses indicate clear-sky values. Units of $\langle CRF_{SW} \rangle$ and $\langle CRF_{LW} \rangle$ are W m^{-2}; $\langle t_{SW} \rangle$ is dimensionless.

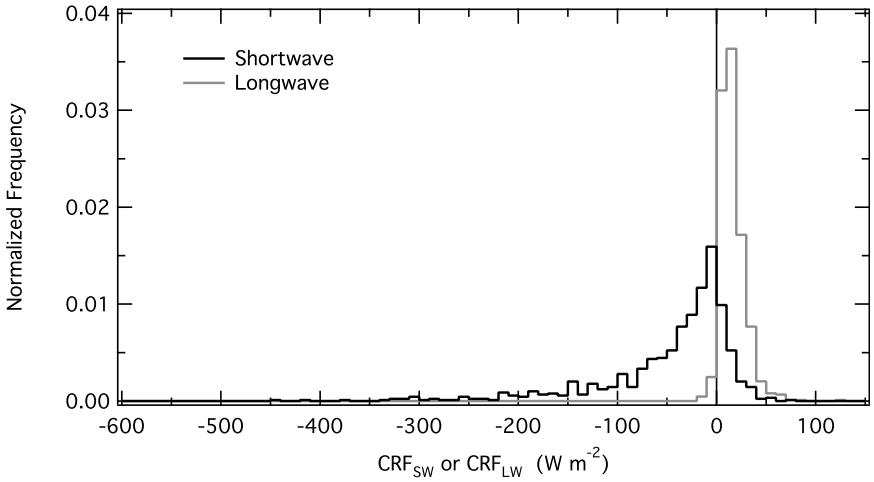

Figure 9. Histogram of hourly average $\overline{\mathrm{CRF}}_{\mathrm{SW}}$ (black) and $\overline{\mathrm{CRF}}_{\mathrm{LW}}$ (gray) for all periods with shallow cumuli.

4.3. Dependence on Cloud Fraction

[26] The $\overline{\mathrm{CRF}}_{\mathrm{SW}}$ is a function of the fractional sky cover determined from the measurements of shortwave radiation. Individual hourly average values of $\overline{\mathrm{CRF}}_{\mathrm{SW}}$ collected over the 201 days are show in Figure 12a. A third-order polynomial has been fit to individual values of $\overline{\mathrm{CRF}}_{\mathrm{SW}}$ (Table 3). This line highlights that the change in $\overline{\mathrm{CRF}}_{\mathrm{SW}}$ with cloud fraction is not linear over the full range of cloud fractions. For additional clarity, the values of $\overline{\mathrm{CRF}}_{\mathrm{SW}}$ have been combined into bins according to the fractional sky cover. The number of hourly averages within each sky cover bin is also a function of the sky cover itself, decreasing from 193 h for cloud fractions between 0.0 and 0.1, to 119 h for cloud fractions between 0.4 and 0.5, and to only 18 h for cloud fractions between 0.7 and 0.8 (Figure 12b). This result is primarily due to our focus on single layer fields of shallow cumuli, where larger cloud fractions are atypical. The small number of hours with sky cover greater than 0.6 contributes to some of the scatter shown in the top of Figure 12a. But the variety of other cloud properties that affect shortwave flux at the surface, such as cloud optical depth and geometry, also contribute to the scatter for a given sky cover.

[27] From the plot of $\overline{\mathrm{CRF}}_{\mathrm{SW}}$ alone, one might speculate that cases with large amounts of clouds make the most significant contribution to the cloud effects on the surface energy budget. The $\overline{\mathrm{CRF}}_{\mathrm{SW}}$ does not, however, account for the number of hours with that specific forcing. In contrast, $\Delta\mathrm{TED}_{\mathrm{SW}}$ (which is the integrated value of $\overline{\mathrm{CRF}}_{\mathrm{SW}}$) accounts for the frequency of occurrence. Thus, moderate amounts of sky cover, which occur much more frequently for the cumulus fields of interest here, can have a larger effect on surface energy budget and climate. These two factors (magnitude of $\overline{\mathrm{CRF}}_{\mathrm{SW}}$ and its occurrence) define $\Delta\mathrm{TED}_{\mathrm{SW}}$, which is also a function of the sky cover (Figure 12c). Rather than plot individual values of $\Delta\mathrm{TED}_{\mathrm{SW}}$, values are determined for sky cover bins, thus $\Delta\mathrm{TED}_{\mathrm{SW}}$ represents the total change in the amount of energy that is available at the surface for a given range of sky cover. The magnitude of $\Delta\mathrm{TED}_{\mathrm{SW}}$ is maximum for moderate sky cover of 0.45.

[28] The value of $\bar{t}_{\mathrm{SW}}$ is also a function of the fractional sky cover. Similar to $\overline{\mathrm{CRF}}_{\mathrm{SW}}$, the $\bar{t}_{\mathrm{SW}}$ decreases nonlinearly

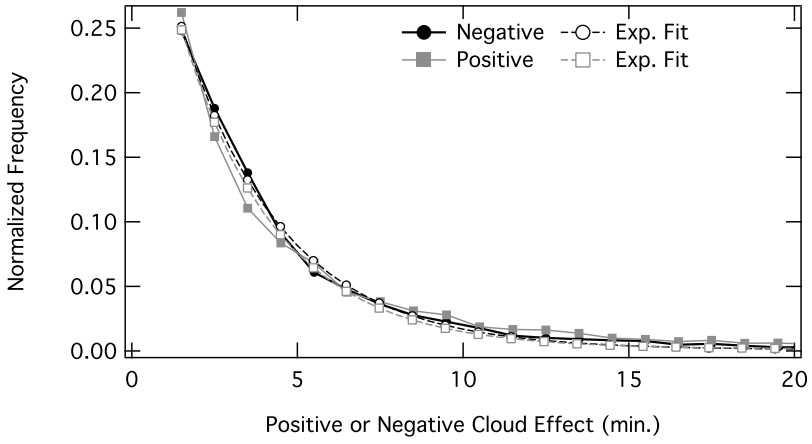

Figure 10. Histogram of the duration of periods with negative (black solid circles) and positive (gray solid squares) cloud effect. Dashed lines indicate an exponential fit to the negative (dashed line with open circles) positive (dashed line with open squares) observations.

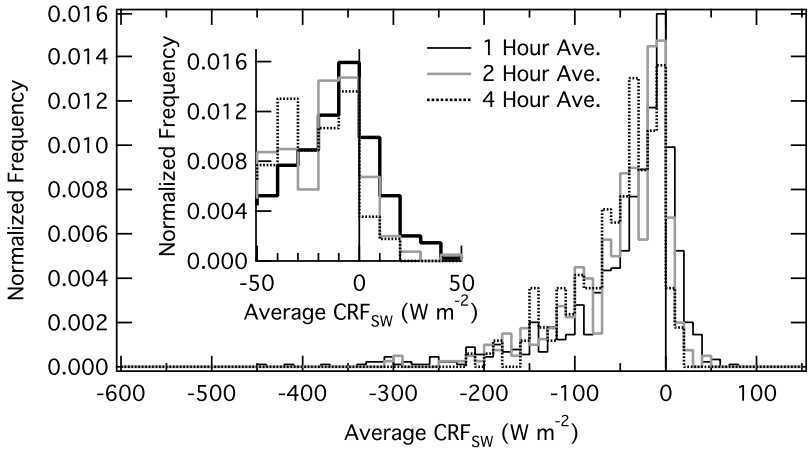

Figure 11. Normalized histograms of $\overline{\mathrm{CRF}}_{\mathrm{SW}}$ computed using averages over 1 h (black), 2 h (gray), and 4 h (dashed line). Inset shows additional detail for values between −50 and 50 W m^{-2}.

with increasing fractional sky cover (Figure 13). This result is expected because of the dependence of both the $\overline{\mathrm{CRF}}_{\mathrm{SW}}$ and $\bar{t}_{\mathrm{SW}}$ on the downwelling F_{SW} and $F_{\mathrm{SW,0}}$. There are also many 1 h averages for which the $\bar{t}_{\mathrm{SW}}$ is greater than 1. This occurs due to the cloud-induced increase in the diffuse component, as discussed in section 3. The nonlinear relationship of both $\overline{\mathrm{CRF}}_{\mathrm{SW}}$ and $\bar{t}_{\mathrm{SW}}$ with C_{SW} is caused by the interplay of two factors: the decrease in the direct radiation reaching the surface and an increase in the diffuse radiation due to enhanced scattering. These factors depend nonlinearly on C_{SW} and the cloud optical depth. The results shown in Figures 12 and 13 do not account for the diurnal variability in the clouds. It is interesting to note that, as reported by *Berg and Kassianov* [2008], the diurnal variability of the cloud fraction of shallow cumuli is due to an increasing number of clouds rather then an increase in the horizontal size of the clouds. They also found that the cloud thickness of shallow cumuli decreases over the day (which is likely associated with a decrease in cloud optical depth), while the cloud fraction tends to be largest in the midafternoon.

[29] The hourly average $\overline{\mathrm{CRF}}_{\mathrm{LW}}$ is found to generally increase with increasing C_{LW} (Figure 14a). In this case, a power law relationship has been fit to $\overline{\mathrm{CRF}}_{\mathrm{LW}}$ to match other results that have appeared in the literature (Table 3). The power law relationship does a good job representing the observations. Individual values of the hourly average $\overline{\mathrm{CRF}}_{\mathrm{LW}}$ have also been sorted into bins of C_{LW}, similar to the treatment of $\overline{\mathrm{CRF}}_{\mathrm{SW}}$. This treatment highlights the trend for $\overline{\mathrm{CRF}}_{\mathrm{LW}}$. As was the case for $\overline{\mathrm{CRF}}_{\mathrm{SW}}$, the total number of observations decrease with increasing C_{LW} (Figure 14b). Thus, the estimates of $\overline{\mathrm{CRF}}_{\mathrm{LW}}$ have a larger uncertainty for larger C_{LW}.

[30] The $\Delta\mathrm{TED}_{\mathrm{LW}}$ provides additional insight into the ways that shallow cumuli impact the longwave surface energy budget. The largest values of $\Delta\mathrm{TED}_{\mathrm{LW}}$ occur for moderate values of C_{LW} (Figure 14c), and the maximum value of $\Delta\mathrm{TED}_{\mathrm{LW}}$ is found for C_{LW} of 0.45. This result is very similar to that found for $\Delta\mathrm{TED}_{\mathrm{SW}}$ (Figure 12c), which also had its maximum for a value of C_{SW} of 0.45. It should be noted, however, that the sky cover was estimated from the longwave and shortwave measurements, respectively. The values of $\Delta\mathrm{TED}_{\mathrm{LW}}$ were computed for all hours with shallow clouds rather than just those hours with more than 48 good 1 min observations (as was used to compute $\overline{\mathrm{CRF}}_{\mathrm{LW}}$). This is the same treatment that was applied for $\Delta\mathrm{TED}_{\mathrm{SW}}$ and explains why values of $\Delta\mathrm{TED}_{\mathrm{LW}}$ are shown

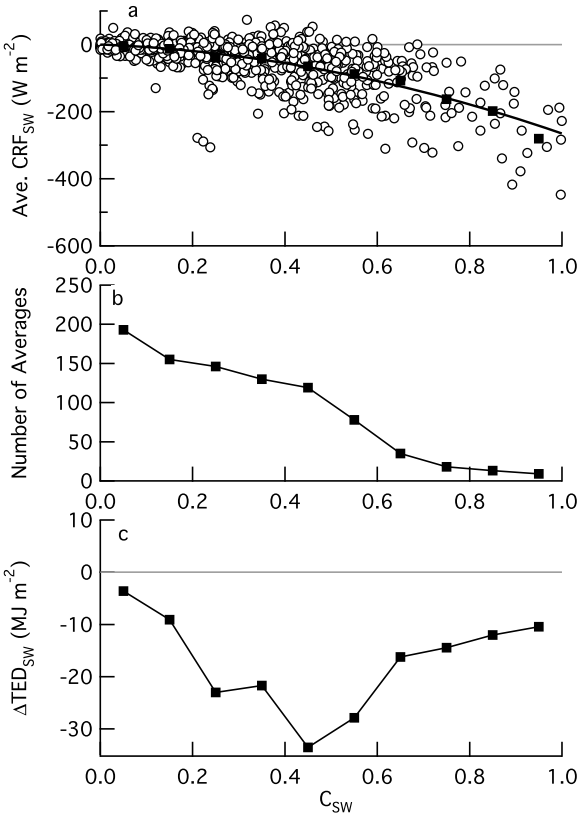

Figure 12. (a) Hourly average $\overline{\mathrm{CRF}}_{\mathrm{SW}}$ (circles) and binned $\overline{\mathrm{CRF}}_{\mathrm{SW}}$ (squares), (b) total number of hourly averages for each sky cover bin, and (c) $\Delta\mathrm{TED}_{\mathrm{SW}}$ as a function of C_{SW} for all hours with shallow cumuli. Line in Figure 12a indicates best fit polynomial to binned values of $\overline{\mathrm{CRF}}_{\mathrm{SW}}$.

Table 3. Fit Parameters for Third-Order Polynomial Fits or Power Law Fits to $\overline{CRF}_{SW}$, $\overline{CRF}_{LW}$, and $\bar{t}_{SW}$ as a Function of C_{SW} and C_{LW}, Respectively

Parameter	Equation
$\overline{CRF}_{SW}$	$\bar{t}_{SW} = -54.64C_{SW} - 210.8C_{SW}^2$
$\overline{CRF}_{LW}$	$\overline{CRF}_{LW} = 6.519C_{LW} - 62.67C_{LW}^{2.170}$
$\bar{t}_{SW}$	$\bar{t}_{SW} = 0.9900 - 0.04918C_{SW} - 0.3346C_{SW}^2$

for values of C_{LW} greater than 0.8 compared to no estimates of $\overline{CRF}_{LW}$ for the same amount of C_{LW}.

5. Discussion

[31] The surface CRF under cloudy conditions is a function of cloud properties including cloud altitude, fractional sky cover, and cloud optical depth. The influence of clouds on the shortwave energy budget is mostly modulated by the cloud fraction and cloud optical depth. Changes in the cloud fraction affect the shortwave energy budget in two ways by changing the frequency with which the direct solar beam reaches the surface and by changing the amount of diffuse radiation. The impacts of clouds on the longwave energy budget are largely a function of the cloud fraction and the cloud base height, which in turn generally determines the cloud infrared radiating temperature.

[32] Seasonal changes in the surface CRF over a specific location occur due to systematic changes in the cloud properties, solar radiation at the TOA, and the surface albedo. The results presented in this study provide a detailed account of changes in the CRF associated with variations in the fractional sky cover of shallow cumuli. The observed cumuli are characterized by low cloud base heights generally ranging from 1.5 to 2 km [e.g., *Berg and Kassianov* 2008] and small cloud optical depths generally less than 10 [e.g., *Chiu et al.*, 2006]. In addition to shallow cumuli, other types of clouds can be found over the ARM SGP Site during the summer [e.g., *Kollias et al.*, 2007], including stratus and stratocumulus that cover the entire sky. Cloud optical depths larger than 30 are frequently observed for overcast conditions at the ARM SGP site [*Barnard and Long*, 2004]. In comparison with cumulus, stratus and stratocumulus are more homogeneous and such homogeneity should lead to a reduced occurrence and magnitude of positive forcing compared to cases with shallow cumuli (sections 3 and 4).

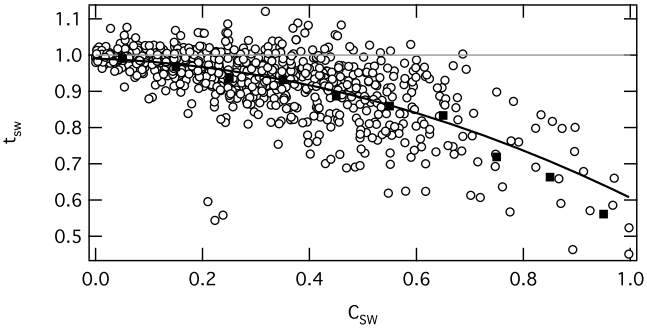

Figure 13. Plot of $\bar{t}_{SW}$ as a function of C_{SW} for all hours with shallow cumuli (circles), binned averages of $\bar{t}_{SW}$(squares), and best fit polynomial to the $\bar{t}_{SW}$ (black line).

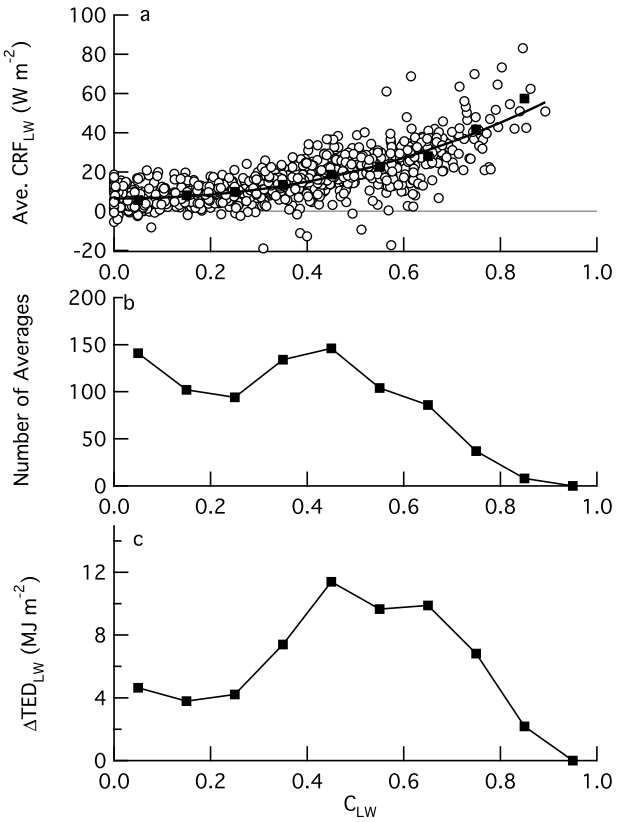

Figure 14. (a) Hourly average $\overline{CRF}_{LW}$ (circles) and binned $\overline{CRF}_{LW}$ (squares), (b) total number of hourly averages for each sky cover bin, and (c) ΔTED_{LW} as a function of C_{LW} for all hours with shallow cumuli. Solid line in Figure 14a indicates power law fit to the binned values of $\overline{CRF}_{LW}$.

[33] To estimate the relative contributions of the cumuli to $\langle CRF_{SW} \rangle$ and $\langle CRF_{LW} \rangle$ at the ARM SGP Site, we compare the corresponding values of cloud radiative forcing obtained for all types of low-altitude clouds [*Dong et al.*, 2006] and shallow cumuli only (Table 2). The results presented by *Dong et al.* [2006] include all types of low-altitude clouds, such as stratus and stratocumulus that cover the entire sky. Contrasting the $\langle CRF_{SW} \rangle$ associated with all low-altitude clouds and cumuli only (Table 2) suggests that the contribution of the shallow cumuli to $\langle CRF_{SW} \rangle$ can be large. The contribution of the shallow cumuli to $\langle CRF_{LW} \rangle$ is more than two times smaller but is also not negligible. Of course, the total radiative impact of the clouds also considers the frequency of occurrence of the clouds, and not just the magnitude of $\langle CRF_{SW} \rangle$. Recall that in section 3, it was reported that single-layer shallow cumuli were observed on 20% of the summertime days. There are also instances in which shallow cumuli could be present along with higher clouds, which would increase the overall frequency of occurrence. There are many areas of the globe where shallow cumuli are much more common, such as regions of the Atlantic, Pacific, and Indian oceans that have frequently occurring trade-wind cumuli.

[34] The $\langle CRF_{LW} \rangle$ is a strong function of both the cloud fraction and the cloud altitude. As documented by *Berg and*

Kassianov [2008], the daily average cloud base height for shallow cumuli at the ARM SGP site is between 1.5 and 2.0 km above ground. *Dong et al.* [2006] required that the cloud top height be less than 3 km to be classified as a low-altitude cloud. Thus, there should be significant overlap in the clouds we define as shallow cumuli and their low-altitude clouds. The $\langle CRF_{LW} \rangle$ is also a function of the fractional sky cover (Figure 14a). Therefore, the differences between $\langle CRF_{LW} \rangle$ values for cases with all low clouds [*Dong et al.*, 2006] and cumuli only (Table 2) could be related to differences in C_{LW} as well. There are very few cases with large C_{LW} (C_{LW} greater than 0.6) in our study (Figure 14b). The magnitude of $\langle CRF_{LW} \rangle$ associated with shallow cumuli is relatively small (Table 2), therefore cumuli play only a small role in the longwave radiation budget.

6. Summary and Conclusions

[35] Small and optically thin shallow cumuli are frequently observed over land and ocean. The geometrical and optical properties of cumulus clouds exhibit large variations over both time and space and lead to a large amount of variability of the radiative properties at the surface. Current large-scale models poorly reproduce this variability partly due the lack of adequate data sets. This study describes the impact of shallow cumuli on the shortwave and longwave components of the CRF at the surface using data collected during eight summers at the ARM SGP site. While the observed quantitative impact on the surface CRF is representative of local conditions at the study site, the qualitative impact, namely the important role of shallow cumuli in the Earth's surface energy budget, is expected to be applicable at a wide range of locations around the globe. The key findings of this study are summarized below.

[36] The summertime averages of the shortwave and longwave components of CRF at the surface are found to be -45.5 W m^{-2} (out of 612 W m^{-2} for clear-sky conditions) and 15.9 W m^{-2} (out of -105 W m^{-2} for clear-sky conditions), respectively. Thus, the shortwave component is nearly 3 times larger than its longwave counterpart and the presence of shallow cumuli lead to a net cooling of the surface. By comparing the summertime averages of CRF obtained for all low-altitude clouds [*Dong et al.*, 2006] and cumuli only (this study) at the ARM SGP Central Facility, we find that cumuli can contribute substantially (approximately 50%) and noticeably (approximately 40%) to the shortwave and longwave CRF associated with all low-altitude clouds, respectively.

[37] The inhomogeneity of the cumulus properties is responsible for many cases with positive shortwave CRF, which are associated with cloud-induced enhancement of the diffuse irradiance. For such cases, the cloudy-sky instantaneous values of the diffuse irradiance may substantially (as large as 225 W m^{-2}) exceed the corresponding instantaneous clear-sky values. The positive and negative components of the shortwave CRF are characterized by the small-scale fluctuations; about 95% of them have less than 20 min duration. In comparison with the positive component of shortwave CRF, the negative component has larger amplitude (up to 800 Wm^{-2}). Although temporal averaging reduces the amplitude of the positive CRF and its population, nearly 20% of all 1 h averages of $\overline{CRF_{SW}}$ were positive. The neglect of the positive component of the forcing would increase the $\langle CRF_{SW} \rangle$ by nearly 24% (from -45.5 to -59.5 W m^{-2}).

[38] The total amount of shortwave and longwave energy deposited at the surface (TED_{SW} and TED_{LW}, respectively) is the amount of energy that is available for partitioning between sensible, latent, and the soil heat flux. Both the ΔTED_{SW} and ΔTED_{LW} have a nonlinear dependence on the fractional sky cover, with the largest values occurring at intermediate sky cover. Two competing factors lead to this behavior of ΔTED_{SW} and ΔTED_{LW}. The first factor is the magnitude of CRF, which increases with increasing sky cover, but for populations of shallow cumuli, instances with large amounts of sky cover occur relatively infrequently. The second factor is the number of occurrences of any cloud amount, which decreases with increasing sky cover for shallow cumuli. These two competing factors lead to the nonlinear behavior of the TED_{SW} and TED_{LW}.

[39] **Acknowledgments.** The comments of two anonymous reviewers significantly improved this manuscript. This work has been supported by the Office of Biological and Environmental Research (OBER) of the U.S. Department of Energy (DOE) as part of the Atmospheric Radiation Measurement (ARM), and Atmospheric Systems Research (ASR) Programs. The Pacific Northwest National Laboratory (PNNL) is operated by Battelle for the DOE under contract DE-AC06-76RLO 1830. D. L. Mills was supported by a DOE Global Change Education Program (GCEP) Summer Undergraduate Research Experience (SURE). Recognition is also extended to those responsible for the operation and maintenance of the instruments that produced the data used in this study; their diligent and dedicated efforts are often underappreciated.

References

Barnard, J. C., and C. N. Long (2004), A simple empirical equation to calculate cloud optical thickness using shortwave broadband measurements, *J. Appl. Meteorol.*, *43*, 1057–1066.

Berg, L. K., and E. I. Kassianov (2008), Temporal variability of fair weather cumulus statistics at the ACRF SGP site, *J. Clim.*, *21*(7), 3344–3358.

Berg, L. K., et al. (2009), Overview of the cumulus humilis aerosol processing study, *Bull. Am. Meteorol. Soc.*, *90*, 1653–1667.

Chiu, J. C., A. Marshak, Y. Knyazikhin, W. J. Wiscombe, H. W. Barker, J. C. Barnard, and Y. Lue (2006), Remote sensing of cloud properties using ground-based measurements of zenith radiance, *J. Geophys. Res.*, *111*, D16201, doi:10.1029/2005JD006843.

Clothiaux, E. E., T. P. Ackerman, G. Mace, K. P. Moran, R. T. Marchand, M. Miller, and B. E. Martner (2000), Objective determination of cloud heights and radar reflectivities using a combination of active remote sensors at the ARM CART sites, *J. Appl. Meteorol.*, *39*, 645–665.

Dong, X., B. Xi, and P. Minnis (2006), A climatology of midlatitude continental clouds from the ARM SGP Central Facility: Part II. Cloud fraction and surface radiative forcing, *J. Clim.*, *19*(5), 1765–1783.

Dupont, J.-C., and M. Haeffelin (2008), Observed instantaneous cirrus radiative effect on surface level shortwave and longwave irradiances, *J. Geophys. Res.*, *113*, D21202, doi:10.1029/2008JD009838.

Durr, B., and R. Philipona (2004), Automatic cloud amount detection by surface longwave downward radiation measurements, *J. Geophys. Res.*, *109*, D05201, doi:10.1029/2003JD004182.

Fairall, C. W., T. Uttal, D. Hazen, J. Hare, M. F. Cronin, N. Bond, and D. E. Veron (2008), Observations of cloud, radiation, and surface forcing in the equatorial eastern Pacific, *J. Clim.*, *21*, 655–673.

Forster, P., et al. (2007), Changes in atmospheric constituents and in radiative forcing, in *Climate Change 2007: The Physical Science Basis. Contribution of Working Group I to the Fourth Assessment Report of the Intergovernmental Panel on Climate Change*, edited by S. Solomon et al., pp. 129–234, Cambridge Univ. Press, Cambridge, U. K.

Franceschini, G. A. (1968), The influence of clouds on solar radiation at sea, *Dtsch. Hydrogr. Z.*, *21*, 162–168.

Ghate, V., B. Albrecht, C. Fairall, and R. Weller (2009), Climatology of surface meteorology, surface fluxes, cloud fraction, and radiative forcing over the southeast Pacific from buoy observations, *J. Clim.*, *22*, 5527–5540.

Hahn, C., and S. Warren (1999), Extended edited synoptic cloud reports from ships and land stations over the globe, 1952–1996, *Tech. Rep. NDP-026C*, Carbon Dioxide Inf. Anal. Cent., Oak Ridge Natl. Lab., Oak Ridge, Tenn.

Jiang, H., G. Feingold, H. H. Jonsson, M. Lu, P. Y. Chuang, R. C. Flagan, and J. H. Seinfeld (2008), Statistical comparison of properties of simulated and observed cumulus clouds in the vicinity of Houston during the Gulf of Mexico Atmospheric Composition and Climate Study (GoMACCS), *J. Geophys. Res.*, *113*, D13205, doi:10.1029/2007JD009304.

Kassianov, E., C. N. Long, and M. Ovtchinnikov (2005), Cloud sky cover versus cloud fraction: Whole-sky simulations and observations, *J. Appl. Meteorol.*, *44*, 86–98.

Kollias, P., G. Tselioudis, and B. A. Albrecht (2007), Cloud climatology at the Southern Great Plains and the layer structure, drizzle, and atmospheric modes of continental stratus, *J. Geophys. Res.*, *112*, D09116, doi:10.1029/2006JD007307.

Lane, D. E., K. Goris, and R. C. J. Somerville (2002), Radiative transfer trough broken clouds: Observations and model validation, *J. Clim.*, *15*, 2921–2933.

Long, C. N. (2005), On the Estimation of clear-sky upwelling SW and LW, paper presented at 15th ARM Science Team Meeting, U.S. Dep. of Energy, Daytona Beach, Fla., 14–18 March.

Long, C. N., and T. P. Ackerman (2000), Identification of clear skies from broadband pyranometer measurements and calculation of downwelling shortwave cloud effects, *J. Geophys. Res.*, *105*(D12), 15,609–15,626, doi:10.1029/2000JD900077.

Long, C. N., and D. D. Turner (2008), A method for continuous estimate of the clear-sky downwelling longwave radiative flux developed using ARM surface measurements, *J. Geophys. Res.*, *113*, D18206, doi:10.1029/2008JD009936.

Long, C. N., T. P. Ackerman, K. L. Gaustad, and J. N. S. Cole (2006), Estimation of fractional sky cover from broadband shortwave radiometer measurements, *J. Geophys. Res.*, *111*, D11204, doi:10.1029/2005JD006475.

Mace, G. G., et al. (2006), Cloud radiative forcing at the atmospheric radiation measurement program climate research facility: 1. Technique, validation, and comparison to satellite-derived diagnostic quantities, *J. Geophys. Res.*, *111*, D11S90, doi:10.1029/2005JD005921.

Miller, M. A., et al. (2007), SGP Cloud and Land Surface Interaction Campaign (CLASIC), *DOE/SC-ARM-0703*, 14 pp., U.S. Dep. of Energy, Washington, D. C.

Pfister, G., R. L. McKenzie, J. B. Liley, A. Thomas, B. W. Forgan, and C. N. Long (2003), Cloud coverage based on all-sky imaging and its impact on surface solar irradiance, *J. Appl. Meteorol.*, *42*, 1421–1434.

Press, W. H., S. A. Teukolsky, W. T. Vetterling, and B. P. Flannery (1996), *Numerical Recipes in C: The Art of Scientific Computing*, 2nd ed., Cambridge Univ. Press, New York.

Ramanathan, V., R. Cess, E. Harrison, P. Minnis, B. Barkstrom, A. Ahmad, and D. Hartmann (1989), Cloud-radiative forcing and climate: Results from the Earth Radiation Budget Experiment, *Science*, *243*, 57–63.

Rauber, R. M., et al. (2007), Rain in (shallow) cumulus over the ocean—The RICO campaign, *Bull. Am. Meteorol. Soc.*, *18*, 1912–1928.

Sengupta, M., E. E. Clothiaux, and T. P. Ackerman (2004), Climatology of warm boundary layer clouds at the ARM SGP Site and their comparison to models, *J. Clim.*, *17*, 4760–4782.

Stull, R. B. (1992), Impact of boundary layer clouds—A case study of cover hours, *J. Clim.*, *5*, 390–394.

Warren, S. G., and C. J. Hahn (2002), Cloud climatology, in *Encyclopedia of Atmospheric Sciences*, edited by J. R. Holton, J. Pyle, and J. A. Curry, pp. 476–483, Academic, New York.

Warren, S. G., C. J. Hahn, J. London, R. M. Chervin, and R. L. Jenne (1988), Global distribution of total cloud cover and cloud type amounts over the ocean, *NCAR Tech. Note NCAR/TN-317+Proc*, 41 pp., Natl. Cent. for Atmos. Res., Boulder, Colo.

Wen, G., R. F. Cahalan, S.-C. Tsay, and L. Oreopoulos (2001), Impact of cumulus cloud spacing on Landsat atmospheric correction and aerosol retrieval, *J. Geophys. Res.*, *106*(D11), 12,129–12,138, doi:10.1029/2001JD900159.

Wyser, K., W. O'Hirok, C. Gautier, and C. Jones (2002), Remote sensing of surface solar irradiance with correction for 3D cloud effect, *Remote Sens. Environ.*, *80*, 272–284.

Xie, S., et al. (2010), ARM climate modeling best estimate data: A new data product for climate studies, *Bull. Am. Meteorol. Soc.*, *91*, 13–20.

L. K. Berg, E. I. Kassianov, and C. N. Long, Pacific Northwest National Laboratory, PO Box 999, Richland, WA 99352, USA. (larry.berg@pnl.gov)

D. L. Mills Jr., Department of Computer Science and Engineering, University of South Carolina, Columbia, SC 29208, USA.